npj | antimicrobials & resistance

Article

https://doi.org/10.1038/s44259-026-00203-w

NV716 acts as an envelope-active adjuvant that enhances antibiotic accumulation in Pseudomonas aeruginosa

Margot Draveny[1,2,4], Hugo Chauvet[2,4], Axelle De Pauw[2], Valérie Rouam[2], Harisa Rista[2], Pierre Legrand[2], Marine Novelli[1], Jean-Michel Bolla[1], Maria Girleanu[3], Anne-Laure Favier[3], Fabienne Neulat-Ripoll[1], Jean-Michel Brunel[1], Frédéric Jamme[2] & Muriel Masi[1,2] ✉

Treatment of Gram-negative infections remains challenging due to limited compound penetration and the presence of efflux mechanisms. *Pseudomonas aeruginosa*, in particular, exhibits strong intrinsic resistance, leaving few effective therapeutic options. Here, we provide mechanistic insight into the activity of NV716, a polyaminoisoprenyl antibiotic adjuvant previously described in Gram-negative bacteria, by linking outer membrane perturbation to quantitative changes in intracellular antibiotic accumulation. In *P. aeruginosa* and *Escherichia coli*, NV716 increased intracellular antibiotic accumulation and potentiated selected antibiotics, with the most pronounced effects observed for doxycycline. Studies using efflux-deficient and porin-mutant strains indicate that NV716 perturbs outer membrane organization, thereby facilitating enhanced intracellular antibiotic accumulation. Population-scale assays revealed increased outer membrane vesicle (OMV) release, and high-resolution imaging visualized membrane-associated alterations and OMV formation. Truncation of the lipopolysaccharide core sensitized *P. aeruginosa* to NV716, consistent with increased accessibility of lipid A. Together, these findings establish a quantitative framework that links controlled outer membrane perturbation to intracellular antibiotic accumulation and antibiotic-class-dependent potentiation.

Antimicrobial resistance (AMR) is a natural process exacerbated by widespread antibiotic use[1,2]. The rise of AMR is a major and serious threat to public health worldwide. Since the introduction of lipopeptides in 2003, there has been little development of new families of antibiotics, while existing drugs are rapidly losing efficacy[3]. In 2016, 700,000 deaths were directly attributed to AMR, and this number is estimated to increase to 10,000,000 by 2050[4]. In 2017, the World Health Organization (WHO) published the first global priority list of bacterial pathogens, identifying 12 antibiotic-resistant bacteria for which new antimicrobials or new therapeutic strategies are urgently needed. Remarkably, 9 of these 12 bacterial superbugs are Gram-negative species, including *Acinetobacter baumannii*, *Pseudomonas aeruginosa*, and *Enterobacterales*[5].

In particular, the discovery of new antibiotics against *Pseudomonas aeruginosa* has proven challenging due to the low accumulation of drugs in these bacteria compared to other Gram-negative pathogens. This is partly due to the lack of non-specific porins, such as OmpF and OmpC, present in *Escherichia coli* and closely related enterobacteria, which facilitate the diffusion of small hydrophilic compounds across the outer membrane with a size restriction of approximately 600 Da[6,7]. In contrast, *P. aeruginosa* has approximately 40 monomeric channels for the transport of specific nutrients, with a size restriction of approximately 200 Da[8,9]. Additionally, *P. aeruginosa* can express a wide range of tripartite efflux pumps, enabling highly efficient antibiotic efflux[10]. These features confer high intrinsic resistance to numerous antibiotics[11,12], including some commonly used to treat infections caused by other Gram-negative pathogens, such as tetracyclines[13]. The observed lack of clinical efficacy of these drugs is attributed to low intracellular accumulation in *P. aeruginosa* rather than a lack of target engagement[12]. The same is true of "Gram-positive only"

[1]INSERM, SSA, MCT, Aix Marseille Univ, Marseille, France. [2]Synchrotron SOLEIL, Saint-Aubin, France. [3]Département Plateformes et Recherche Technologique, Institut de Recherche Biomédicale des Armées (IRBA), Bretigny-sur-Orge, France. [4]These authors contributed equally: Margot Draveny, Hugo Chauvet. ✉e-mail: muriel.masi@univ-amu.fr

antibiotics (e.g., macrolides, oxazolidinones, glycopeptides, or rifamycins), which are inactive against Gram-negative pathogens. Consequently, only four classes of antibiotics (β-lactams, fluoroquinolones, aminoglycosides, and polymyxins) are currently employed in clinical settings to treat *P. aeruginosa* infections[13]. Furthermore, the emergence of resistance and the toxicity of certain classes of agents (e.g., polymyxins and aminoglycosides)[14,15], underscore the need to develop novel antibacterial agents.

Several approaches are being developed to increase the intracellular concentration of antibiotics in Gram-negative pathogens, including efflux inhibition[16–18] and outer membrane disruption[19–21] by using non-antibiotic compounds. These combination approaches should help extend the life of our existing antibiotic arsenal and fill the gaps in discovering new antibacterial compounds. Therefore, efforts have been made to synthesize new adjuvants with improved safety profiles and enhanced efficacy. Among them, the polyaminoisoprenyl compound NV716 proved capable of restoring the activity of several antibiotics in Gram-negative bacteria, including *P. aeruginosa*[22–25]. No stable resistance to NV716 could be selected after serial passages at subinhibitory concentrations, but transcriptomic analysis showed the upregulation of genes involved in the lipopolysaccharide (LPS) biosynthesis[26]. This suggests that NV716 targets the LPS organization or biogenesis. However, investigations into the mode of action of NV716 have been inconclusive in identifying a specific target[26]. Furthermore, it remained unclear whether the data on potentiation of antibacterial activities could be linked to increased accumulation of antibiotics in bacteria.

For several years, our group and others have investigated antibiotic activity and intracellular accumulation in *E. coli* and *P. aeruginosa*, establishing correlations between physicochemical properties and accumulation capacity in relation to membrane architecture in these species[27–32]. In this study, we evaluated the effect of NV716 on the accumulation of two representative antibiotics, ciprofloxacin (CIP) and doxycycline (DOX), in *E. coli* and *P. aeruginosa*. Using isogenic efflux pump and porin knock-out mutants, we observed that NV716 does not measurably alter efflux activity under the tested conditions but is associated with changes in outer membrane permeability, particularly enhancing DOX accumulation in *P. aeruginosa*. High-resolution imaging further revealed membrane-associated alterations and increased outer membrane vesicle release at concentrations of NV716 that correlated with antibiotic potentiation. In addition, truncation of the LPS core sensitized *P. aeruginosa* to NV716, consistent with altered accessibility of lipid A within the outer membrane. Preliminary evaluation in a *Galleria mellonella* infection model did not demonstrate a statistically significant improvement in survival under the tested conditions, although a trend toward increased survival was observed. Finally, the implications of selective outer membrane modulation for the design of polyamine-containing antibiotic derivatives are discussed.

Results

NV716 enhances antibiotic activity in association with increased intracellular accumulation independently of detectable efflux inhibition

The efficacy of compound NV716 was evaluated at a concentration of 10 μM in combination with a panel of antibiotics representing diverse classes (tetracyclines, quinolones, macrolides, chloramphenicol, and rifampicin) against wild-type strains of *P. aeruginosa* and *E. coli* K12 (Tables 1 and S2). We observed a potentiation of antibiotic activity in the presence of NV716, although not across the entire antibiotic spectrum. For example, the MIC of tetracyclines (i.e., doxycycline, DOX, and minocycline against PAO1 and AG100, respectively) decreased 128-fold, while that of fluoroquinolones (i.e., ciprofloxacin, CIP, and enrofloxacin against both PAO1 and AG100) only decreased to 4-fold. Interestingly, NV716 also resulted in a 16-fold reduction in the MIC of nalidixic acid, chloramphenicol, and rifampicin. Among these, nalidixic acid and rifampicin are hydrophobic antibiotics that cannot cross bacterial outer membranes via porins and demonstrate limited penetration across LPS[33–35]. Conversely, chloramphenicol, tetracyclines, and fluoroquinolones may be taken up by the porin or the lipid pathway in *E. coli*[34–36]. Still, they are also substrates for efflux pumps in both *E. coli* and *P. aeruginosa*[37–40].

Table 1 | Potency of NV716 in combination with different classes of antibiotics against *P. aeruginosa* PAO1

Antibiotic	MIC (μg/ml)	MIC with NV716 (μg/ml)	Potentiation (fold)
Doxycycline	64	0.5	128
Minocycline	32	0.5	64
Ciprofloxacin	0.5	0.25	2
Enrofloxacin	1	0.25	4
Nalidixic acid	256	8-16	16-32
Erythromycin	256	64	4
Chloramphenicol	64	4	16
Rifampicin	32	2	16

Potentiation of antibiotics was carried out in the presence of 10 μM NV716. The MIC of NV716 against *P. aeruginosa* PAO1 is 50 μM.

Given that NV716 potentiation is observed across several classes of antibiotics, it was postulated that this compound may act via a common mechanism against Gram-negative bacteria. To gain insight into its potential target, we hypothesized that NV716 could inhibit drug efflux or disrupt the integrity of the outer membrane, two key barriers that limit antibiotic accumulation in Gram-negative bacteria. Accordingly, we examined the impact of NV716 on antibiotic accumulation in wild-type strains of *E. coli* K12 and *P. aeruginosa* and derivative efflux knock-out strains using the fluorescence properties of fluoroquinolones (CIP) and tetracyclines (DOX). The efflux knock-out strain of *P. aeruginosa* is devoid of the six operons that encode the constitutive and dormant RND-type efflux pumps, while that of *E. coli* only lacks AcrB, which is essential for the function of the major AcrAB-TolC efflux system in this species.

The accumulation of CIP was measured by spectrofluorimetry in bacterial lysates after 15 min of drug exposure. The SICAR (Structure-Intracellular Concentration-Activity Relationship) index has been proposed for quantifying the accumulation of fluoroquinolones and other antibiotics[41]. Specifically, the $SICAR_{(EFF)}$ index is calculated as the ratio between the average number of antibiotic molecules accumulated in strains with and without efflux, thus reflecting the sensitivity of a given antibiotic to this accumulation barrier. In *E. coli*, CIP showed a $SICAR_{(EFF)}$ of 1.5 when AcrB was genetically or chemically inactivated in the presence of the protonophore carbonyl cyanide (m-chlorophenyl) hydrazone (CCCP)[30], but a $SICAR_{(EFF)}$ of 1.0 when cells were exposed to NV716 (Fig. S1A). Similarly, CIP showed a $SICAR_{(EFF)}$ of 2.75-3.0 in the absence of active efflux in *P. aeruginosa*, but a $SICAR_{(EFF)}$ of 1.15 in the presence of NV716 (Fig. 1A). Consistent with the previous MIC results, NV716 does not measurably alter CIP accumulation under the tested conditions in these bacterial species. Furthermore, since active efflux has a significant effect on CIP accumulation, it is unlikely that NV716 acts as an efflux pump inhibitor.

Tetracyclines, including DOX, are fluorescent antibiotics whose intensity increases as they enter bacterial cells[41]. This property was used to monitor the accumulation of DOX in intact bacterial populations over time by using spectrofluorimetry. In contrast to ciprofloxacin, doxycycline accumulation responded immediately to NV716 exposure in *P. aeruginosa* (Fig. 1B). This was also observed in the efflux knock-out mutant (Fig. S1B), supporting the conclusion that NV716 activity is independent of detectable efflux inhibition. The presence of polymyxin B (PMB) was also found to enhance DOX accumulation, indicating that both compounds enhance DOX accumulation through OM perturbation, although their mechanisms of action differ in magnitude and membrane selectivity. In this case, the decrease in fluorescence intensity after a sharp increase may reflect membrane destabilization at this concentration (Fig. 1B). In *E. coli*, tetracyclines

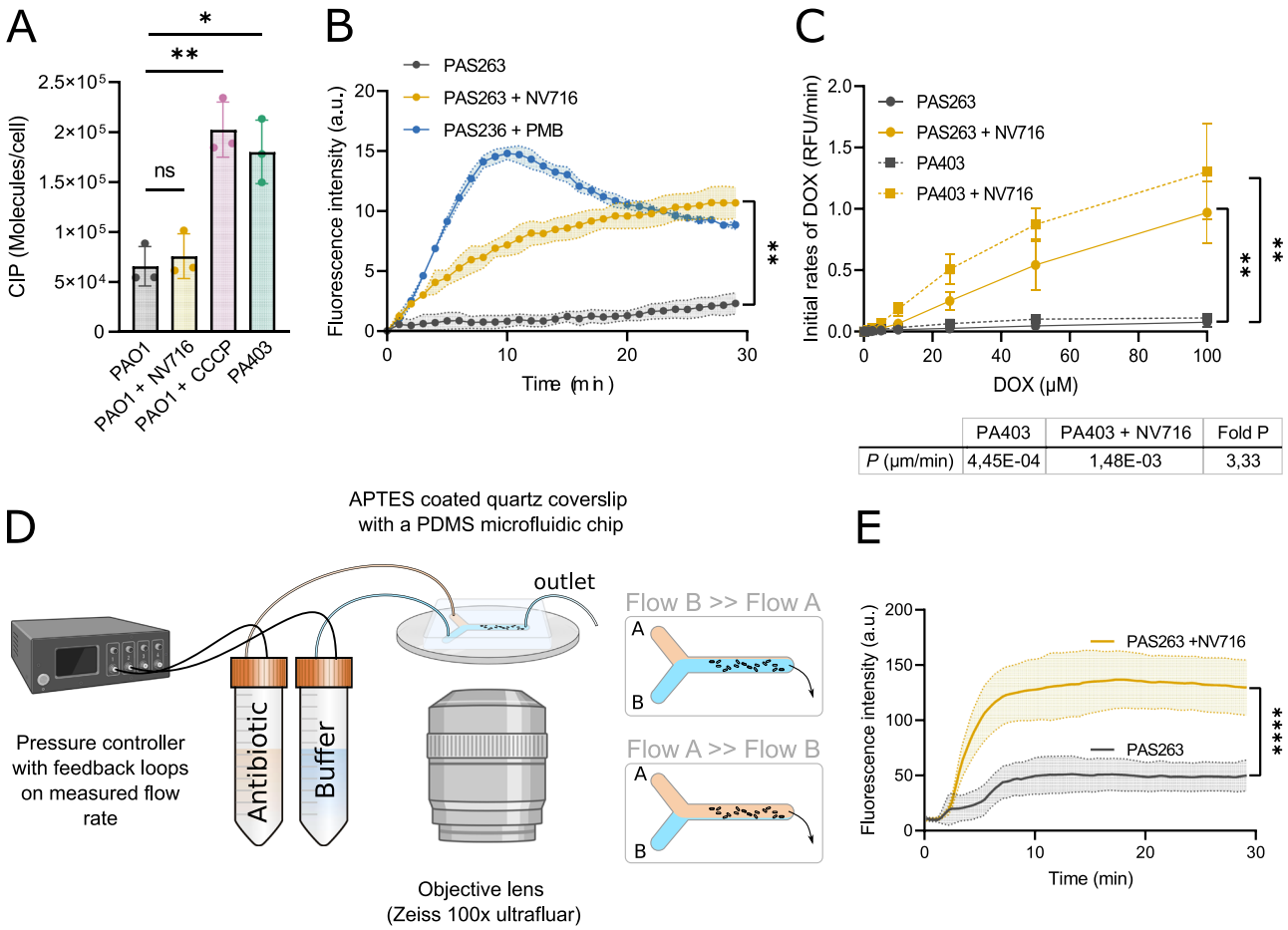

Fig. 1 | NV716 increases the accumulation of some antibiotics in *P. aeruginosa*. **A** Accumulation of CIP in *P. aeruginosa* using UV fluorescence. The graph shows the intracellular amount of antibiotic (average number of molecules per bacteria) in PAO1 (wild-type, Efflux$^+$) and PA403 (Efflux$^-$) after a 15-minute incubation with CIP. Quantification of CIP (molecules/cell) in each bacterial population was determined using spectrofluorimetry. Each point represents an individual biological replicate. Data are presented as mean ± standard deviation (SD) from three independent experiments ($n = 3$). Individual data points underlying the graphs are provided in Supplementary Data 1. One-way ANOVA was used to compare the means in CIP of each bacterial population to PAO1 (**$P < 0.01$; *$P < 0.05$; ns non-significant $P \geq 0.05$ by Dunnett's multiple comparison test). **B** Real-time accumulation of DOX in *P. aeruginosa* at the population level using UV fluorescence. The final concentration of DOX and NV716 was 100 μM and 10 μM, respectively. Each point represents the mean value obtained from independent experiments (PAS263, $n = 6$; PAS263 + NV716, $n = 3$; PAS263 + PMB, $n = 3$). The line represents the mean fluorescence signal over time, and the shaded area indicates ±SD. Individual data points underlying the graphs are provided in Supplementary Data 1. Fluorescence intensities of DOX accumulation in bacterial populations of PAS263 and PAS263 + NV716 at $t = 30$ min were used for statistical analysis. An unpaired t-test with Welch correction was used to compare the means in antibiotic accumulation between these conditions (**$P < 0.01$). **C** Accumulation kinetics of DOX in *P. aeruginosa* PAS263 (Efflux$^+$) and PA403 (Efflux$^-$). The graph shows the relationship between the initial accumulation rates (V_{in}) and the extracellular concentration (C_0) of DOX. Accumulation experiments for each extracellular concentration of DOX were repeated in three independent biological experiments ($n = 3$). Data are presented as mean ± SD, and individual data points are provided in Supplementary Data 1. Values of V_{in} at $C_0 = 200$ μM were used for statistical analysis. An unpaired t-test with Welch correction was used to compare the means in antibiotic accumulation between each pair of conditions (**$P < 0.01$). The table shows the outer membrane permeability (P, μm/min) of PA403 calculated as described in "Methods". Fold P was calculated as the gain of outer membrane permeability of PA403 in the presence of NV716. **D** The left panel shows the microfluidic chamber assembly (see "Methods" for a complete description). The right panel shows the switch between the buffer and the antibiotic solutions in the microfluidic chamber. Created in BioRender with a free trial plan. **E** Accumulation of DOX was monitored in single cells of PAS263 by using time-resolved DUV-fluorescence imaging for 30 min. Images were analyzed and corrected as described in "Methods". Fluorescence intensities of DOX accumulation in single cells at t = 30 min were used for statistical analysis. Data corresponds to individual cells analyzed from two independent experiments (PAS263, $n = 65$ cells; PAS263 + NV716, $n = 77$ cells). Data are presented as mean ± SD. Individual data points underlying the graphs are provided in Supplementary Data 1. An unpaired t-test with Welch correction was used to compare the means in antibiotic accumulation between the two conditions (****$P < 0.0001$).

cross the outer membrane via porin channels[36]. Consistently, NV716 increases DOX accumulation solely in experiments conducted with porin knock-out strains, in which the *ompF* and *ompC* genes have been deleted (AG100ΔFC and AG100AΔFC) (Fig. S1C, D).

Subsequently, assays were conducted with varying DOX concentrations to measure DOX accumulation kinetics (Fig. 1C). We found that the initial accumulation rates (V_{in}) in *P. aeruginosa* strains are minimal and exhibit a slow and minimal increase with external antibiotic concentration (C_0). Conversely, the presence of NV716 resulted in a notable increase in V_{in} as the concentration of doxycycline increased. At a concentration of 100 μM, DOX accumulates ~12.5 times faster and ~4.5 times more in both wild-type and efflux knock-out strains in the presence of NV716 (Fig. 1C). A comparable phenomenon was observed in *E. coli* strains that do not express OmpF and OmpC porins. However, the impact of NV716 is less pronounced in *E. coli* than in *P. aeruginosa*, as evidenced by the rate of DOX accumulation at a similar extracellular concentration (~2–3 times faster in both AG100ΔFC and AG100AΔFC) (Fig. S1E). This difference is consistent with the higher intrinsic membrane permeability of *E. coli* compared to *P.*

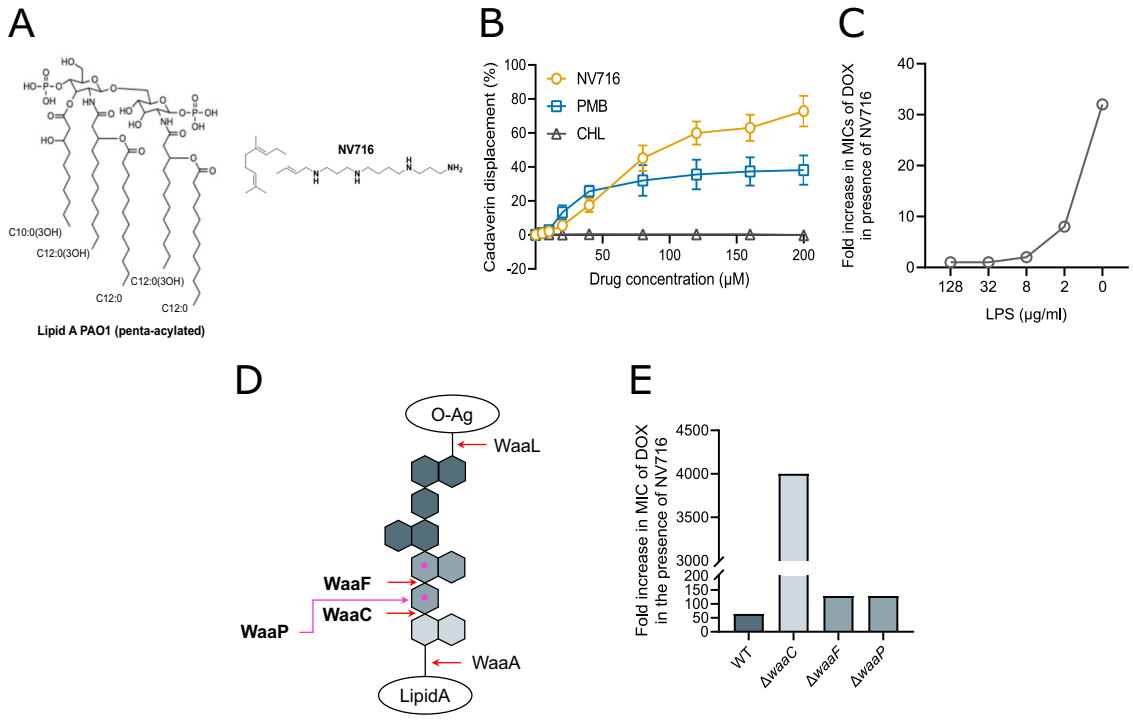

Fig. 2 | NV716 exerts activity by interacting with LPS. A Structure of penta-acylated lipid A of *P. aeruginosa* PAO1 and NV716[23]. **B** BC-LPS displacement assay. The BC probe binds to LPS and quenches its fluorescence. Compounds binding LPS displace the probe and restore its fluorescence. The graph shows dose-dependent increases in BC fluorescence in the presence of PMB (positive control) and NV716, but not CHL (negative control). Data represents the mean ± SD from four independent biological experiments ($n = 4$). Individual data points underlying the graphs are provided in Supplementary Data 2. **C** Exogenous addition of LPS impairs the potentiation of DOX activity by NV716 in a dose-dependent manner. Data represents the median values from three independent biological experiments ($n = 3$). Individual data points underlying the graphs are provided in Supplementary Data 2. **D** Schematic representation of the bacterial LPS: light blue-gray represents Kdo residues; mid and dark blue-gray represent the inner and the outer core residues of the LPS oligosaccharide (OS) moiety, respectively. *Waa* genes are responsible for adding the OS core residues to the LPS precursor and phosphorylation reactions (pink asterisks). Here, the loss of WaaF or WaaP prevents the addition of heptose II or phosphorylation of heptose I, respectively. The loss of WaaC leads to the formation of $(Kdo)_2$-lipid A. **E** NV716-dependent potentiation of DOX activity against *P. aeruginosa* mutants displaying various modifications in the LPS OS core moiety. Data represent the median values from four independent biological experiments ($n = 4$). Individual data points underlying the graphs are provided in Supplementary Data 2.

aeruginosa (i.e., the initial DOX accumulation rates were approximately six times higher in *E. coli* than in *P. aeruginosa* in the absence of NV716). As detailed in "Methods", the combination of these experiments with a first-order diffusion model allowed for the estimation of the gain in membrane permeability (P in μm/min) of DOX in the presence of NV716. The membrane permeability of DOX without NV716 is substantially lower in *P. aeruginosa* PA403 compared to *E. coli* AG100A. In the presence of NV716, the permeability of PA403 increases by a factor of ~3.5, reaching a value comparable to the one estimated for AG100A in the absence of NV716 (Figs. 1C and S1E).

We complemented the measurements above with studies on isolated bacteria of wild-type *P. aeruginosa* using a DUV-microscopy assay. We have previously described the development of kinetic microspectrofluorimetry to quantify antibiotic accumulation in isolated bacteria over time[41]. However, resuspended bacteria deposited between two quartz coverslips are often mobile, and their resuspension with the drug away from the microscope prevents recording of the fluorescence signal at the beginning of the experiment. To overcome these shortcomings, we developed a flexible, easy-to-assemble, and accessible microfluidics system (Fig. 1D). As with spectrofluorimetry, NV716 induced a significant and rapid increase in DOX accumulation in *P. aeruginosa* (Fig. 1E). The plateau was reached in less than 10 min in microscopy compared to 30 min in spectrofluorimetry, most likely because of the phenotypic heterogeneity of antibiotic accumulation in cells at the population scale. Parameters calculated in the presence of NV716 also show differences, such as total DOX accumulation (RFU at $t = 30$ min), which is 5-fold greater in spectrofluorimetry versus 2.5-fold in microscopy, and DOX accumulation kinetics (RFU/min), which is 15-fold faster in spectrofluorimetry (Fig. 1B) versus 6.25-fold in microscopy (Fig. 1E).

Taken together, the data are consistent with NV716 inducing perturbation of outer membrane organization, thereby facilitating the penetration of DOX. This also suggests that the main barrier to the accumulation and antibacterial activity of DOX is the low permeability of the outer membrane in this species.

It is noteworthy that NV716 has previously been reported to potentiate doxycycline activity against multidrug-resistant (MDR) clinical isolates of *P. aeruginosa* (Table S3)[42]. The present study further supports an association between antibiotic potentiation and increased intracellular accumulation, as reflected by the sensitization of clinical isolates to doxycycline in the presence of NV716 and the corresponding increase in intracellular accumulation (Fig. S2). These findings warrant further investigation of NV716-doxycycline combinations in physiologically relevant infection models.

NV716 interacts with LPS at the bacterial cell surface

We proceeded to examine the interactions between NV716 and LPS—the major outer membrane surface component—using *P. aeruginosa* as a model organism (the molecular structures of NV716 and PAO1 lipid A are depicted in Fig. 2A). First, we used a previously described LPS binding assay with the BODIPY-tagged cadaverine (BC) probe, which binds to lipid A phosphate groups. The binding of molecules to LPS results in a displacement of the BC probe, which in turn increases its fluorescence intensity. Here, NV716 showed a dose-dependent capacity to displace BC from its binding to purified P. aeruginosa LPS. This effect was greater than PMB and CHL, selected as LPS-targeting and non-LPS-targeting antibiotics,

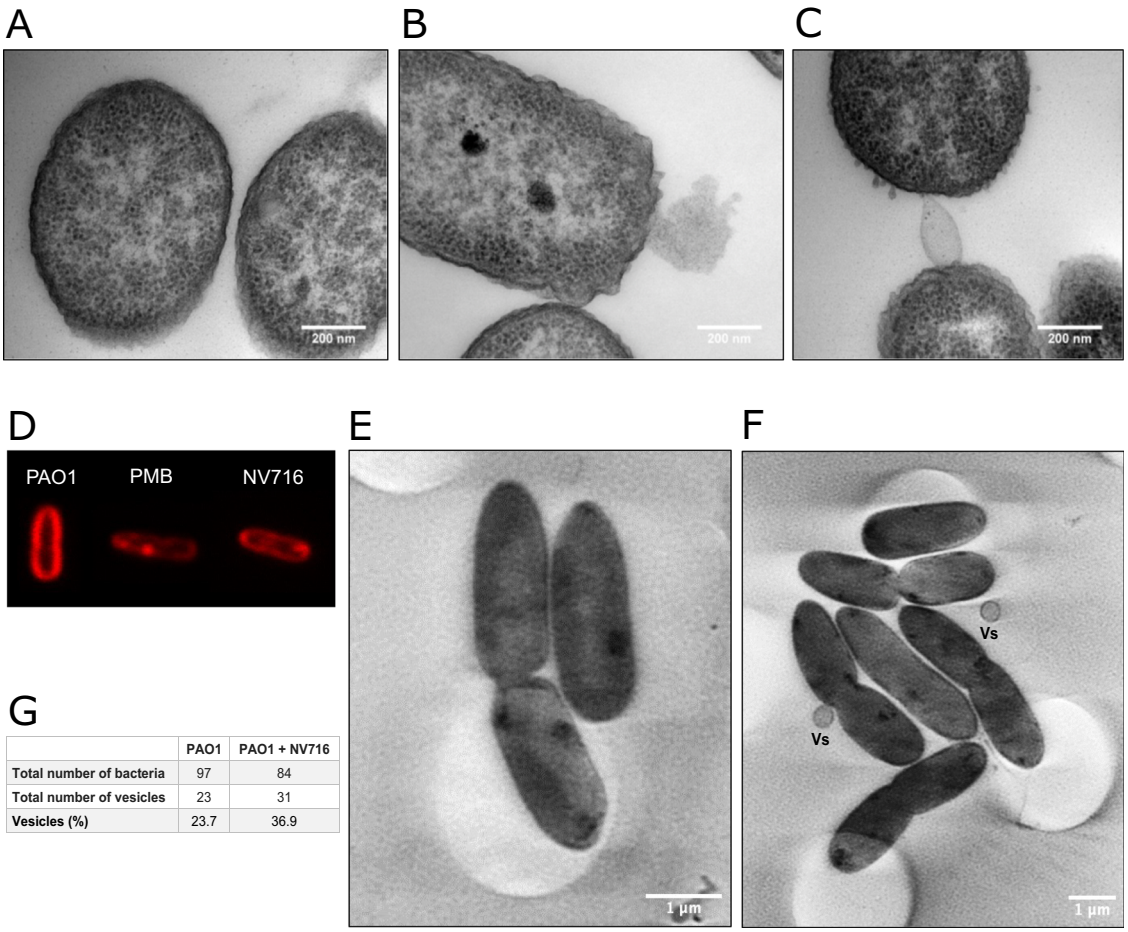

G

	PAO1	PAO1 + NV716
Total number of bacteria	97	84
Total number of vesicles	23	31
Vesicles (%)	23.7	36.9

Fig. 3 | NV716 disrupts the outer membrane integrity of *P. aeruginosa* and enhances the production of bacterial vesicles. TEM micrographs of *P. aeruginosa* PAO1 in control conditions without NV716 (**A**) and after 30 min exposure to NV716 (**B**, **C**). Scale bar: 200 nm. **D** Fluorescence microscopy of *P. aeruginosa* cells stained with FM4-64. Cells were untreated (left) or exposed to PMB (1 µM, middle) or NV716 (10 µM, right). Deconvoluted cryo-soft X-ray tomographic slices of *P. aeruginosa* PAO1 in control conditions without NV716 (**E**) and after 30 min exposure to NV716 (**F**). Scale bar: 1 µm. Vesicles (Vs) emerging from the bacterial surface are indicated. TEM and cryo-SXT experiments were independently repeated twice. **G** Enumeration of bacteria and bacterial vesicles observed in cryo-SXT tomograms. A total of 97 and 84 bacteria were counted from 20 and 22 tomograms for PAO1 in the absence and presence of NV716, respectively. Statistical analysis was performed using an unpaired two-tailed t-test ($P = 0.2297$, ns).

respectively (Fig. 2B). Then, on adding exogenously purified LPS of *P. aeruginosa*, we observed a dose-dependent inhibition of the antibacterial activity for the combination of DOX and NV716 (Fig. 2C). Interestingly, NV716 failed to potentiate the accumulation of DOX when cells were incubated in the presence of high concentrations of Mg^{2+} (data not shown), which promotes electrostatic interactions between adjacent LPS molecules through the lipid A moiety. These observations are compatible with a possible electrostatic competition with Mg^{2+} at the level of lipid A. Consistent with this, NV716 was previously shown to activate the PhoPQ two-component system[26], which is stimulated in Mg^{2+}-limiting conditions and upon challenge with cationic peptides[43,44].

To refine the location of this interaction within the LPS architecture, we analyzed the ability of NV716 to potentiate DOX in *P. aeruginosa* mutants expressing truncated variants of the oligosaccharide (OS) core. We observed that a deep truncation in the OS core, such as in a *waaC* mutant that only produces KDO_2-lipid A LPS molecules, resulted in enhanced potentiation, consistent with increased accessibility of lipid A in these truncated LPS mutants (Fig. 2D, E).

A previous study determined the capacity of NV716 (i) to permeabilize the outer membrane with the measurement of 1-N-phenylnaphthylamine (NPN) fluorescence, (ii) to permeabilize both the outer and the inner membranes with the measurement of propidium iodide (PI) fluorescence when getting access to intracellular DNA, and (iii) to depolarize the inner membrane with the measurement of $DiSC_3(5)$ fluorescence[26]. The results showed that NV716 produced a significant increase in NPN fluorescence but only modest changes in PI and $DiSC_3(5)$ assays[26]. Overall, the data indicate that NV716 induces outer membrane perturbation consistent with LPS interaction, while producing no visible effects on inner membrane integrity.

NV716 is associated with outer membrane perturbation and increased outer membrane vesicle release

The impact of NV716 on the morphology of *P. aeruginosa* was initially investigated by transmission electron microscopy (TEM). The morphological alterations associated with NV716 treatment were the release of bacterial vesicles or membrane patches and the formation of high electron-density intracellular granules (Fig. 3A–C).

Fluorescence microscopy with the membrane dye FM4-64 confirmed the accumulation of membrane-like material in the form of bright foci at the cell surface of bacteria exposed to PMB or NV716 (Fig. 3D).

The chemical composition of the electron-dense granules was investigated. Based on previous reports, these structures are consistent with polyphosphate (PolyP) granules, inorganic phosphate polymers involved in bacterial stress responses[45–47]. The *P. aeruginosa* genome encodes multiple polyphosphate kinases, including Ppk1 and Ppk2A, which are essential for PolyP synthesis[47]. Energy dispersive X-ray spectroscopy (EDX) confirmed

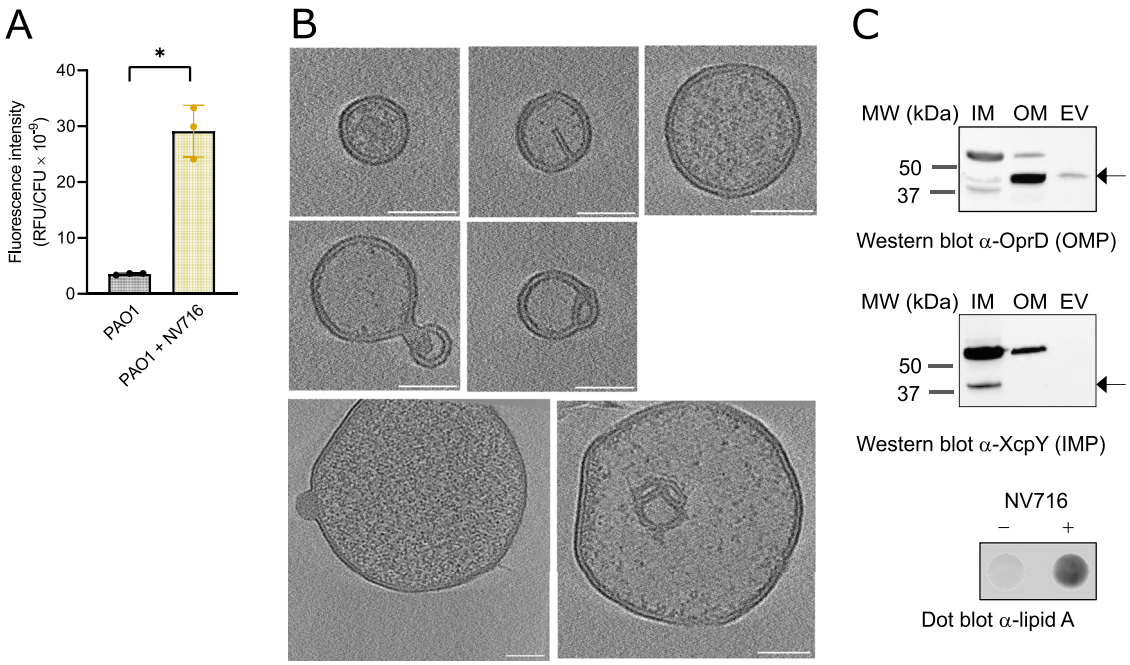

Fig. 4 | *P. aeruginosa* releases outer membrane vesicles upon exposure to NV716. **A** Bacterial vesicles were collected and quantified from cultures of PAO1 untreated or treated with 10 µM NV716 and quantified. Data are presented as mean ± SD from three independent biological experiments ($n = 3$). Individual data points underlying the graphs are provided in the Supplementary Data 3. Statistical analysis was performed using an unpaired t-test with Welch correction ($^*P < 0.05$). **B** Cryo-EM images of vesicles isolated from NV716-treated cultures. Scale bar: 50 nm. **C** Immunodetection of OprD, XcpY, and lipid A in vesicles isolated from NV716-treated cultures by Western blot and Dot blot analyses.

the presence of phosphorus-enriched granules in wild-type PA14 under nitrogen-deficient conditions, which were absent in the corresponding Δ*ppk* mutant, supporting their identification as PolyP (Fig. S3A, B and Table S4). PolyP granules were detected in both PAO1 and PA14 following NV716 exposure (Fig. S3C–F). Despite their clear visualization, quantitative analysis did not reveal a significant increase in PolyP production upon treatment (Table S5), indicating that NV716 does not measurably stimulate PolyP synthesis under the tested conditions. Notably, morphological alterations were more pronounced in Δ*ppk* mutants exposed to NV716 (Fig. S4), suggesting that PolyP-associated phenotypes may modulate the cellular response to membrane stress, although the underlying mechanism remains unresolved.

To gain further insight into the alterations in bacterial ultrastructure in response to NV716, we used cryo-soft X-ray tomography (cryo-SXT). Cryo-SXT is a technique that permits imaging of unstained and cryopreserved biological samples. Furthermore, cryo-SXT offers nanoscale resolution (~30 nm) and high-carbon contrast for investigating the precise organization of membrane structures and other intracellular components of biological samples. In particular, we sought to investigate the release of membrane-like material in *P. aeruginosa* PAO1 exposed to NV716, as previously observed by TEM. As described in "Methods", cryo-SXT tilt-series were collected to examine the 3D structure of bacteria that had been treated or untreated with NV716. A series of reconstructed tomogram slices is presented for comparison of the two conditions (Fig. 3E, F). The bacterial double membrane is visible, though this technique is unable to differentiate between the inner and outer membranes. Extracellular vesicles can also be observed, with some emerging directly from the bacterial surface (Fig. 3F). The total number of vesicles observed in tomograms corresponding to both conditions suggests increased vesicle abundance in NV716-treated samples (Fig. 3G). However, this number is likely underestimated due to the collection of bacteria by centrifugation before deposition on the grids and the sample blotting process before vitrification. To complement these observations at the single-cell level, we adapted the growth conditions of *P. aeruginosa* PAO1 with or without NV716 to isolate, quantify, and characterize extracellular vesicles at the population scale. Vesicles collected from culture supernatants were first quantified by spectrofluorimetry using the FM4-64 membrane dye. Addition of NV716 resulted in a marked increase in vesicle production (~8.5-fold; Fig. 4A).

Precise ultrastructural imaging data of the hydrated vesicles were then obtained by cryo-electron microscopy. Two electron-dense layers were observed (Fig. 4B); however, the intermembrane distance (~3 nm) is incompatible with the dimensions of the periplasm, arguing against classical outer-inner membrane vesicles. Additionally, vesicles displayed considerable heterogeneity in both diameter (50–500 nm) and morphology.

SDS-PAGE analysis revealed the presence of proteins in vesicles isolated from NV716-treated cultures, including a prominent band corresponding to the outer membrane porin OprD. Western blot analysis confirmed the presence of OprD but not the inner membrane protein XcpY (Fig. 4C, upper and middle panels). Dot blot analysis using an anti–lipid A antibody further confirmed the presence of LPS in vesicles collected from NV716-treated cells (Fig. 4C, lower panel).

To further assess vesicle composition, double staining with FM4-64 and DAPI was performed. No detectable DNA-associated fluorescence was observed in NV716-induced vesicles under the tested conditions, although signal intensity was limited (data not shown). Taken together, these results indicate that NV716 exposure is associated with increased outer membrane vesicle release.

NV716 localizes in the bacterial membranes

A copper-labeled derivative of NV716 (Cu-NV716) was synthesized and used for cryo-X-ray fluorescence nano-imaging (nano-XRF). This derivative retained DOX potentiation activity against *P. aeruginosa* PAO1 under the tested conditions (see "Methods"). Nano-XRF enabled nanoscale (~20 nm) mapping of elemental distribution in close-to-native conditions. Phosphorus mapping revealed a homogeneous intracellular signal consistent with nucleic acid distribution (Fig. S5A, C). In contrast, copper fluorescence was enriched at the periphery of Cu-NV716-treated bacteria rather than uniformly distributed throughout the cytoplasm (Fig. S5B, D).

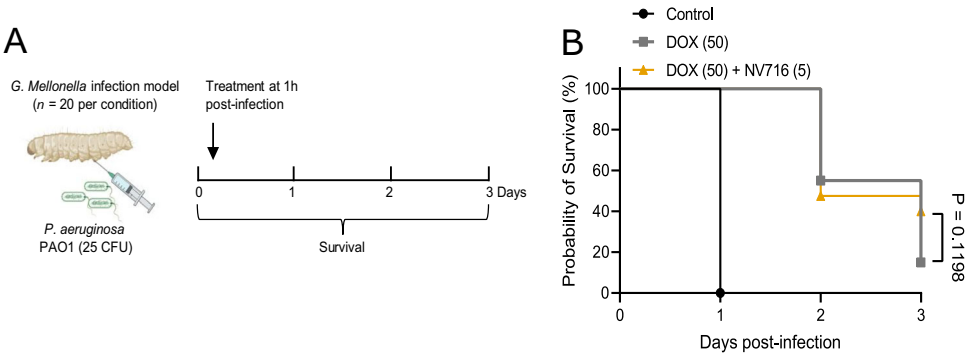

Fig. 5 | NV716 does not significantly enhance doxycycline activity in the *G. mellonella* infection model under the tested conditions. A Scheme of the experimental protocol. Larvae were randomly assigned to treatment groups ($n = 20$ biologically independent animals per condition). Created in BioRender with a free trial plan. **B** Survival rates of *G. mellonella* larvae infected with *P. aeruginosa*. Larvae were infected with PAO1 and treated with doxycycline (50 mg/kg) alone or in combination with NV716 (5 µM). Survival was monitored for three days. Each group contained 20 biologically independent larvae ($n = 20$). Statistical significance was determined using a two-sided log-rank (Mantel–Cox) test. Individual survival data underlying the graph are provided in Supplementary Data 4.

Given the penetration of X-rays through the entire cell volume, this peripheral enrichment is consistent with the membrane-associated localization of Cu-NV716.

Evaluation of NV716-doxycycline combination in a preliminary *Galleria mellonella* model

The sensitization of *P. aeruginosa* to DOX in the presence of NV716 was further assessed using the *G. mellonella* (wax moth) infection model (Fig. 5A). As shown in Fig. 5B, larvae treated with the combination of DOX and NV716 showed a trend toward increased survival compared to DOX alone; however, this difference did not reach statistical significance under the tested conditions.

To further explore the physicochemical properties of NV716, complementary in silico ADMET predictions were performed using the ADMETlab server (Supplementary Data 8)[48]. NV716 exhibited a predicted LogP of 5.73 and a topological polar surface area (TPSA) of 62.11, values consistent with membrane interaction. Predicted plasma protein binding (~65%) and intestinal absorption parameters suggest moderate systemic exposure. While classified as a potential P-glycoprotein inhibitor, NV716 retained predicted oral bioavailability above 30%. ADMETlab analysis indicated no major genotoxic, cytotoxic, or hemotoxic liabilities in silico; however, these predictions require experimental validation. Overall, these analyses provide preliminary insight into the physicochemical profile of NV716, which is currently positioned as a proof-of-concept envelope-active adjuvant.

Discussion

Bacterial resistance to antibiotics remains a major public health challenge, exacerbated by the scarcity of new compounds. Among WHO-prioritized pathogens, Gram-negative bacteria are particularly problematic due to their impermeable outer membranes, reinforced by reduced porin expression and efflux pump activity, which together confer multidrug resistance. In response to these resistances, developing compounds that target the outer membrane is an obvious strategy. Among the approaches studied, new antibiotic development focuses both on biogenesis machinery and the structure of the outer membrane[49]. An alternative to developing entirely new antibiotics is the use of adjuvant compounds, whose mechanisms of action may include efflux inhibition[50] or outer membrane permeabilization[51,52], thereby restoring antibiotic accumulation and activity and/or creating new sensitivities.

In this study, we investigated the adjuvant NV716 and its impact on the intracellular accumulation of doxycycline and ciprofloxacin in *E. coli* and *P. aeruginosa*, both critical Gram-negative pathogens. NV716 sensitized *P. aeruginosa* to doxycycline, with a clear correlation between intracellular accumulation and antibacterial activity. Extending these findings, we had previously examined a series of tetracycline derivatives and found that NV716 broadened the chemical space compatible with antibacterial activity, enabling more hydrophobic compounds to accumulate and exert activity by altering the rules of outer membrane permeation[53].

Mechanistically, NV716 increases outer membrane permeability in a manner consistent with interaction with lipopolysaccharides, without causing overt structural damage. Recent studies revealed that polymyxins, the best-known LPS-targeting antibiotics, permeabilize both the outer and inner membranes and act by targeting LPS that has trafficked to the inner membrane[54]. In contrast, NV716 acts exclusively at the cell surface. This was confirmed using two complementary assays. First, nitrocefin degradation assays demonstrated that NV716, like polymyxin B, permeabilizes the outer membrane and promotes access to periplasmic β-lactamases (Fig. S7A, B). Second, propidium iodide staining revealed that, in contrast to polymyxin B, NV716 does not compromise inner membrane integrity, as no PI-positive cells were detected following exposure (Fig. S7C, D). These effects were consistently observed in both *P. aeruginosa* and *E. coli*, indicating that NV716 selectively perturbs the outer membrane without inducing secondary damage to the inner membrane. This surface-restricted activity likely contributes to its lower cytotoxic potential and supports its development as a membrane-targeting antibiotic adjuvant.

Notably, NV716 exposure is associated with increased release of OMVs. As OMV production is a well-established bacterial response to envelope stress, the increased vesiculation observed here is interpreted as a consequence of membrane perturbation rather than as a NV716-specific biogenesis pathway. Indeed, OMVs may contribute to population-level adaptation by modulating interactions with the extracellular environment. From a biotechnological perspective, this phenomenon opens the possibility of screening the polyaminoisoprenoid chemolibrary—from which NV716 was originally identified—to discover additional species-specific compounds that promote OMV release. Such compounds could serve as versatile platforms for functional studies of outer membrane proteins in their native environment, offering new avenues for mechanistic and structural investigations.

Unexpectedly, our ultrastructural analyses also revealed the presence of inorganic polyphosphate (PolyP), a polymer increasingly recognized as a central metabolic and stress-related signaling molecule. PolyP granules are synthesized by polyphosphate kinases (PPKs), which convert ATP to PolyP, and this process is dynamically regulated to buffer cellular energy and stress. NV716-induced morphological alterations appeared more pronounced in mutants lacking PPKs, indicating that PolyP may influence the bacterial response to envelope stress, although the underlying mechanism remains unclear. This is consistent with recent studies reporting that PPK1 activity influences LPS structure and contributes to polymyxin resistance[55]. However, our analysis of lipid A with and without NV716 did not reveal detectable modifications, suggesting that any PolyP-associated effects are unlikely to involve canonical lipid A remodeling (Fig. S8). Future work will

be required to clarify the contribution of PolyP to the cellular response induced by NV716.

Our findings also highlight broader principles governing antibiotic accumulation in Gram-negative bacteria. While *E. coli* accumulation follows the eNTRY rules[28]—requiring ionizable nitrogen, low three-dimensionality, and moderate rigidity—*P. aeruginosa* relies on distinct PASsagE parameters, with compounds traversing the LPS layer rather than porins[32,56]. Indeed, NV716 facilitates antibiotic entry by altering outer membrane organization, as supported by quantitative accumulation measurements, enhancing the accumulation of otherwise poorly permeant antibiotics. A similar principle was demonstrated by Hergenrother et al. with a polyamine-fusidic acid chimera, in which the polyamine motif enhanced both membrane perturbation and compound accumulation[32]. Therefore, this concept supports the rational design of chimeric molecules combining a membrane-perturbing moiety with a non-permeant antibiotic, currently under development.

Preliminary in vivo evaluation in the *G. mellonella* infection model did not demonstrate a statistically significant improvement in survival with the NV716–doxycycline combination under the conditions tested. These data highlight the need for further investigation in optimized infection models to assess the potential in vivo relevance of membrane-mediated antibiotic potentiation. In parallel, in silico ADMET predictions indicate physicochemical properties compatible with further preclinical evaluation, although experimental validation will be required. Future studies will therefore aim to evaluate NV716 and related derivatives in physiologically relevant infection models to determine whether the quantitative enhancement of intracellular antibiotic accumulation observed here can translate into measurable therapeutic benefit, including models relevant to respiratory and skin infections.

Overall, our work demonstrates that targeted modulation of outer membrane permeability can expand the range of compounds active against Gram-negative pathogens, providing a framework for developing next-generation adjuvants as species-specific antibiotic potentiators.

Methods

Bacterial strains, growth conditions, and chemicals

All strains are listed in Table S1. Unless stated otherwise, bacterial strains were grown aerobically in Luria Bertani (LB) broth at 37 °C to the mid-exponential phase (optical density at 600 nm, OD_{600} ~ 0.6). Pyoverdine, the primary siderophore produced by *P. aeruginosa*, exhibits a strong absorption peak at 400 nm[57]. Consequently, we used PAS263, a PAO1-derived mutant incapable of synthesizing pyoverdine[58] for DOX accumulation experiments. PA403 was grown under conditions of excess iron (LB supplemented with 10 mM $FeSO_4$) to minimize pyoverdine production. Commercially available chemicals for routine use were purchased from Sigma-Aldrich. Specific grade chemicals for electron microscopy were purchased from Electron Microscopy Sciences. NV716 was synthesized as described previously[24]. The chemical synthesis of NV716 coupled to copper (Cu-NV716) is detailed in a subsequent section.

Drug susceptibility assays

Minimum inhibitory concentrations (MICs) were determined by the standard 2-fold microdilution method in 96-well microplates according to the guidelines of the CLSI (http://clsi.org). Cultures were grown in Mueller-Hinton II broth, and approximately 2×10^5 cells were distributed into each well. After an incubation of 18 h at 37 °C, bacterial growth was evaluated using the 2-(4-iodophenyl)-3-(4-nitrophenyl)-5-phenyl-2H-tetrazolium chloride (INT) reduction test. Experiments were carried out in triplicate ($n = 3$) and expressed as the resulting median values.

Accumulation of ciprofloxacin

Accumulation assays were performed as previously described[41]. Briefly, bacteria were grown to the mid-exponential phase, collected by centrifugation (5000 × *g*, 15 min, 21 °C), and resuspended in NaPi buffer (50 mM NaH_2PO_4/Na_2HPO_4, pH 7.4, 2 mM $MgCl_2$) to a final density of 6×10^9 Colony Forming Units (CFU) per ml. A set volume (0.8 ml) of each bacterial suspension was incubated without or with drugs (CIP, 5 µM; NV716, 10 µM; CCCP, 10 µM) for 15 min at 37 °C. Then, a set volume (0.8 ml) of each condition was mixed with NaPi buffer (1.1 ml), and the bacterial pellets were immediately collected by centrifugation (10,000 × *g*, 5 min, 4 °C).

Preparation of bacterial lysates and determination of ciprofloxacin intracellular concentration by spectrofluorimetry

Bacterial lysis was achieved with 500 µl of 0.1 M Glycin-HCl (pH 3.0) overnight at room temperature. Bacterial debris was removed by centrifugation (10,000 × *g*, 15 min, 4 °C). Four hundred microliters of each clear lysate was mixed with 600 µl of Glycin-HCl, and 100 µl of each sampled lysate was placed in black half-wells of a 96-well microplate (Greiner Bio-One). Fluorescence emission spectra were recorded with a Spark® TECAN microplate reader with the following wavelengths: excitation at 275 nm and emission collected from 300 to 500 nm. In each sample, the antibiotic fluorescence maximum intensity (λ_{Em} ~ 450 nm) was corrected by the tryptophan maximum intensity fluorescence (λ_{Em} ~ 340 nm)[41]. The average number of antibiotic molecules per bacterial cell was determined as described previously[41]. Data were expressed as means and standard deviations from three independent assays ($n = 3$).

Monitoring accumulation kinetics of doxycycline in intact bacteria at the population level

Bacteria were grown to the mid-exponential phase, collected by centrifugation, and resuspended in NaPi buffer to an optical density at 600 nm (OD_{600}) of 0.6. To limit time loss at t_0, 10 µl of DOX (for final concentrations of 0, 1.25, 2.5, 5, 10, 25, 50, and 100 µM) were first added into wells of a clear-bottomed, black-edged microplate (Greiner Bio-One), followed by 10 µl of NaPi buffer ± NV716 or PMB (10 µM final), and 180 µl of bacterial suspension. The fluorescence of DOX was immediately measured using a Spark® TECAN microplate reader at one-minute intervals for 30 min, with the following wavelengths: excitation at 400 nm and emission at 520 nm. The readout was reported as DOX fluorescence (arbitrary units, a.u.), which is the relative fluorescence calculated by subtracting the intrinsic fluorescence of bacteria alone. To estimate the changes in outer membrane permeability due to NV716, we assumed that the slow diffusion across the outer membrane is the most limiting factor for antibiotic transport in the absence of active efflux (e.g., in PA403 and AG100A). In this case, a first-order model based on Fick's law of molecular diffusion could be written as: $(dC_{in}/dt) \times V = -P \times S \times [C_0 - C_{in}(t)]$, where V is the bacterial volume (µm³), S is the bacterial cell surface (µm²), P is the outer membrane permeability (µm/min), C_0 is the extracellular concentration of DOX, C_{in} is the intracellular concentration of DOX, and dC_{in}/dt is the variation of the intracellular concentration of DOX over time (i.e., the accumulation rate becomes the influx rate for bacteria strains without efflux). In the initial phase of drug exposure, the extracellular concentration of DOX is largely above the intracellular concentration ($C_{in} \ll C_0$). Consequently, the aforementioned first-order model can be effectively simplified as follows: $(dC_{in}/dt) \times V = -P \times S \times C_0$. The influx rate ($dC_{in}/dt$) could then be evaluated to estimate the outer membrane permeability P, assuming that DOX fluorescence is proportional to its intracellular concentration ($dI_{in}/dt \propto dC_{in}/dt$, with I_{in} the intracellular fluorescence intensity). Finally, a linear regression analysis was performed to examine the accumulation of DOX fluorescence during the initial phase ($t = 5$ min). The surface and volume of the bacteria were estimated by Desmarais et al. [59]. To verify that the influx rate (in RFU/min) is proportional to the extracellular concentration (C_0), accumulation experiments were repeated with varying extracellular concentrations of DOX. These experiments were repeated at least three times in independent assays, and the accumulation or influx rate was expressed as the mean and standard deviation.

Fabrication of microfluidic devices

A master of the canal pattern was made on a silicon wafer using a SU-8 2050 resin (MicrochemTM) and was engraved with the Dilase 250 laser

lithography system. The main channel was 0.6 mm wide, 7 mm long, and 100 µm thick. The polydimethylsiloxane (PDMS) silicone SylgardTM 184 was mixed with a curing agent (ratio 10:1). The mixture was degassed, poured onto the wafer, and dried at 75 °C overnight. Chips were detailed in PDMS and punched at entries and exits with a 0.3 mm diameter core sampler (EMS rapid core). In parallel, quartz coverslips were coated by immersion for 1 h with 3% APTES in ethanol. Microfluidic chips were individually plasma-bonded on top of APTES-coated quartz coverslips.

DUV imaging of doxycycline accumulation kinetics in single cells and data analysis

Bacteria were grown to the mid-exponential phase, collected by centrifugation, and resuspended in NaPi buffer to an OD_{600} of 1. The bacterial suspension was introduced into the microfluidic chip via one of the two available inlets and allowed to settle for 10 min. Thereafter, the chip was washed with NaPi buffer, which was introduced through the same inlet. Each of the two entries of the chip was connected to a NaPi or a DOX (100 µM) ± NV716 (10 µM) reservoir, respectively. The flow rate was set to 20 µl/min for the buffer and 1 µl/min for the drug(s) using a pressure controller (OB1 MK4 from ELVESYS). The chip was then positioned on the inverted microscope (a UV-modified homemade Zeiss Axio Observer Z-1, equipped with a Zeiss ultrafluar objective with 100 X magnification, 1.25 NA) of the DISCO beamline at SOLEIL Synchrotron[60,61]. Two distinct regions of interest (ROIs) were delineated in the brightfield before the start of data acquisition for 30 min with measurement intervals of one minute and acquisition times of 5 s for DOX fluorescence and 100 milliseconds for brightfield images. The switch between the "NaPi buffer" to the "DOX ± NV716" entries was initiated remotely 2 min after the start of the recording. The antibiotic fluorescence was collected through a 480-–550 nm bandpass filter following UV excitation between 320 nm and 380 nm, using a bandpass filter. Images were processed to extract the fluorescence kinetics in each bacteria using a Python script (https://gitlab.synchrotron-soleil.fr/disco-beamline/bacteria-drug-uv-analysis). The images were stabilized, and the bacteria were segmented for each time step using the StarDist algorithm[62], which was trained on images of DUV antibiotic accumulation acquired on the DISCO beamline. The segmented bacteria were then tracked with the STracking library (https://github.com/sylvainprigent/stracking). Finally, the average intensity of fluorescence was extracted for each tracked bacterium.

BODIPY-cadaverine displacement assay

The BODIPY-cadaverine (BC, Thermo Fisher Scientific) displacement assay was performed as previously described[63] to quantify the binding affinities of PMB, NV716, and chloramphenicol (CHL, negative control) to rough-type type LPS (from *P. aeruginosa* strain 10, L9143, Sigma-Aldrich). The fluorescence of BC is quenched upon binding to LPS, and displacement by the test compounds increases fluorescence intensity. PMB, NV716, and CHL solutions were prepared 2× and serially diluted in NaPi buffer. A solution of 10 µM BC and 200 µg/ml R-LPS was prepared in the same buffer and incubated for 15 min in the dark. Finally, 50 µL of BC-LPS mixtures were added to the black half-wells of a 96-well microplate containing 50 µl of the serially diluted compounds. After an incubation of 30 min in the dark, the fluorescence intensity was read with a Spark® TECAN microplate reader with the following wavelengths: excitation at 580 nm and emission at 620 nm.

Outer membrane disruption assay

Bacteria were grown to the mid-exponential phase. Imipenem was then added (0.125 µg/mL for PAO1 and 0.35 µg/mL for AG100_AmpC and AG102_AmpC), followed by incubation at 37 °C for 1 h under agitation. Cells were then washed in potassium phosphate buffer (20 mM K_2HPO_4, 1 mM $MgCl_2$, pH 7.0) and resuspended to an OD_{600} of 0.5 for AG100_AmpC or 0.375 for PAO1. Aliquots of 100 µl of each suspension were transferred to wells of a transparent 96-well microplate containing the test compound (10 µM final) and nitrocefin (0.2 mg/ml). Nitrocefin hydrolysis was monitored at 37 °C by measuring absorbance at 490 nm using an Infinite Pro200 microplate reader (Tecan). The microplate was incubated with shaking (180 r.p.m.) at 37 °C for 60 min, and absorbance was measured every minute. Data were reported by calculating the mean area under the curves (AUC).

Inner membrane disruption assay

Bacteria were grown to the mid-exponential phase. Cells were then washed in NaPi buffer and resuspended to an OD_{600} of 0.5. Aliquots of 100 µl of each suspension were transferred to wells of a black-walled microplate containing the test compound (10 µM final) and propidium iodide (2.5 mM final). Fluorescence was measured immediately in a Tecan Infinite 200 Pro multiwell plate reader (excitation at 535 nm, emission at 620 nm). The microplate was incubated with shaking (180 r.p.m.) at 37 °C for 85 min, and fluorescence (excitation at 535 nm, emission at 620 nm) was measured every 15 min. Data were reported by calculating the mean area under the curves (AUC).

Transmission electron microscopy

Bacteria were grown to the mid-exponential phase, collected by centrifugation (5000 × *g*, 15 min, 21 °C), and resuspended in NaPi buffer to an OD_{600} of 0.6 ± NV716 (10 µM final). After an exposure time of 30 min, bacteria were pelleted by centrifugation (10,000 × *g*, 5 min, 4 °C). Bacteria were fixed with 2.5% (v/v) glutaraldehyde in cacodylate buffer (0.1 M, pH 7.4) overnight at 4 °C. After washing, samples were postfixed with 1% (v/v) osmium tetroxide in cacodylate buffer for 1 h at room temperature under a chemical hood and covered with aluminum foil. Then, samples were stained for 1 h at 4 °C with 2% (v/v) uranyl acetate and dehydrated at different ethanol concentrations. Samples were embedded in Epon LX112 (Inland Europe) resin and subjected to polymerization for 48 h at 60 °C. Ultrathin sections with a thickness of 80 nm were cut with an ultramicrotome Reichert Ultracut S (Leica Microsystems) and placed onto 300 mesh copper grids. Sections were double-stained with 2% uranyl acetate and lead citrate as a standard contrast technique for electron microscopy. High-resolution TEM was performed with a CM10 microscope operating at 100 keV and equipped with a charge-coupled device (CCD) Erlanghsen 1000 Gatan camera. No filtering was applied to the images.

Scanning transmission electron microscopy and energy-dispersive X-ray spectroscopy

Control experiments were performed using *P. aeruginosa* PA14 and a derivative mutant incapable of synthesizing polyphosphate (Supplementary Table 1) as described in Racki et al. [47]. For nitrogen starvation experiments, strains were grown at 37 °C shaking in MOPS-buffered minimal media overnight (40 mM sodium succinate, 22 mM NH_4Cl, 43 mM NaCl, 2.2 mM KCl, 1.25 mM NaH_2PO_4, 1 mM $MgSO_4$, 0.1 mM $CaCl_2$, 7.5 µM $FeCl_2$, 0.8 µM $CoCl_2$, 0.5 µM $MnCl_2$, 0.5 µM $ZnCl_2$, 0.2 µM Na_2MoO_4, 0.1 µM $NiCl_2$, 0. 1 µM H_3BO_3, and 0.01 µM $CuCl_2$, 50 mM MOPS, pH 7.2). Cultures were grown to mid-exponential phase, spun down, and resuspended in nitrogen-limited MOPS-buffered minimal media identical to MOPS-buffered media, but with 1 mM NH_4Cl—for 1 h. Other experiments were performed with PAO1 grown to mid-exponential phase in LB and exposed to NaPi buffer ± NV716 as described for TEM analyses. Samples used for STEM-EDX analysis were prepared as described above for TEM analysis. Ultrathin sections with a thickness of 120 nm were cut and deposited on Ni grids without negative staining to avoid chemical modifications. STEM-EDX analyses were performed on a Titan Themis 300 G3 microscope (Thermo Fisher Scientific) equipped with an extreme field emission gun (X-FEG) electron source module and operated at 300 keV. TEM images were acquired using an FEI CMOS Ceta 16 M camera, while the high-angle annular dark-field (HAADF) and bright-field (BF) detectors were used for STEM image acquisition. EDX spectra were collected from regions of interest (ROIs) using an X-Max 80T silicon drift detector and analyzed with the AZtec software platform (Oxford Instruments).

Cryo-soft X-ray tomography and image analysis

Bacteria were grown to the mid-exponential phase, collected by centrifugation, and resuspended in NaPi buffer to an OD_{600} of 0.6 ± NV716 (10 µM final). After an exposure time of 30 min at 37 °C, bacteria were pelleted by centrifugation (10,000 × *g*, 5 min, 4 °C) to remove N716 and resuspended in NaPi buffer. Two microliters of bacterial suspension were deposited on the carbon side of holey carbon-coated gold Quantifoil® gold finder grids R2/2 (Au G200F1, Quantifoil Micro Tools) freshly glow-discharged with plasma (15 mA for 90 s). Two microliters of 100 nm gold beads (GC100, BBI solutions) were then deposited over the drop containing bacteria and used as fiducial markers for projections alignment to common axis for rotation before tomographic reconstruction. Grids were vitrified at −180 °C in liquid ethane using a Leica GP automatic plunge freezer (Leica Microsystems), then blotted for 2 s on the gold side to remove the excess media using Whatman® blotting paper. Experiments were conducted on the transmission X-ray tomography beamline MISTRAL at ALBA Synchrotron[64]. The incoming beam energy was set to 520 eV, and a 25 nm Fresnel zone plate was used, resulting in a pixel size resolution of 10 nm. A series of tilts was performed, with projections collected from −65° to +65° at an angular step of 1° and an exposure time of 2 s for each projection[65]. The tilt series were initially corrected for the incoming flux and subsequently deconvolved with a Wiener filter, utilizing the point spread function of the optical setup[66]. These tilt series were aligned with a patch-tracking technique using AreTomo[67] and IMOD[68]. The aligned tilt series were then reconstructed using the SIRT (Simultaneous Iterative Reconstruction Technique) algorithm implemented in the Tomo3D software[69] with an iteration parameter of 40. In addition, two images at 0° angle were taken before and after the tilt series acquisition to ensure that the sample was not damaged by the X-ray beam.

Fluorescence microscopy

Bacteria were grown to the mid-exponential phase and exposed to NV716 (10 µM final) or PMB (1 µM final) as described for TEM and cryo-SXT analyses. Bacteria were collected by centrifugation, resuspended in 500 µl of NaPi with 5 µg/ml FM 4-64 (Thermo Fisher Scientific). After 5 min at 4 °C in the dark, the cells were pelleted, washed, and resuspended in NaPi buffer. Two microliters were spotted between two glass coverslips and observed using an inverted fluorescence microscope (OLYMPUS IX83) at 100X magnification. The mCherry (λ_{ex} = 542–582 nm; λ_{em} = 603–678 nm) filter was used to visualize the FM4-64 fluorescence. Images were collected on a CCD camera using µManager[70].

Isolation and quantification of extracellular vesicles

Overnight cultures were used to inoculate 500 ml of LB at a 1:100 dilution and grown at 37 °C to mid-exponential phase (OD_{600} ~ 0.4). Cells were collected by centrifugation (10,000 × *g*, 10 min) and resuspended in the same volume of fresh LB with or without NV716 (10 µM final). All cultures were then allowed to grow at 37 °C until they reached an OD_{600} of 0.9–1.1. An aliquot of each culture was assessed for growth on agar plates to determine bacterial viability, expressed as CFU/ml. Cultures were subjected to centrifugation (10,000 × *g*, 10 min), and the resulting supernatant was sterilized through filtration with a polyethersulfone membrane of 0.45 µm (Thermo Fisher Scientific). Subsequently, extracellular vesicles in the cell-free supernatants were collected by centrifugation (38,000 × *g*, 1 h, 4 °C), washed once in HEPES buffer (50 mM, pH 6.8), and filtered again. The samples were then concentrated by ultracentrifugation (120,000 × *g*, 1 h) and resuspended in 100 µl of HEPES buffer. The quantity of vesicles was assessed by using the lipophilic fluorophore FM4-64 (Thermo Fischer Scientific). Fluorescence was recovered in half-well black microplates with a Spark® TECAN microplate reader with the following wavelengths: excitation at 506 nm and emission at 550 nm, to obtain relative fluorescence units per milliliter (RFU/ml). The number of RFU/ml was then divided by the number of CFU/ml determined at the time of vesicle harvest to generate the vesicle yield (RFU/CFU). The RFU/CFU of vesicle preparations from treated cultures was then divided by the RFU/CFU of vesicle preparations from untreated cultures to determine the fold of vesicle induction.

Cell fractionation

Bacteria were grown to an optical density at 600 nm (OD600) of 1.0 and collected by centrifugation (6000 × *g*, 20 min). The cell pellet of a 100 ml culture was resuspended in 5 ml NaPi buffer. The bacterial cells were lysed using a one-shot cell disruptor (Constant Systems Ltd.) at 2 kbar. Unlysed cells were removed by low-speed centrifugation (8000 × *g*, 20 min, 4 °C), then the supernatant was ultracentrifuged at 120,000 × *g* for 1 h. The pellet, corresponding to total membranes, was resuspended in 3 ml NaPi buffer containing 0.3% (v/v) N-lauryl-sarcosinate (Sigma Aldrich). After 30 min of solubilization at room temperature, the outer and inner membranes were separated by ultracentrifugation (120,000 × *g*, 1 h). The supernatants corresponding to the solubilized inner membrane and the pellet corresponding to the outer membrane were saved and stored at −20 °C until use. The outer membrane pellets were directly resuspended in Laemmli buffer, whereas the supernatants, which contained soluble or inner membrane proteins, were precipitated with 20% trichloroacetic acid (v/v). The loading was adjusted to an equivalent of 1.0 OD unit for protein analysis.

SDS-PAGE and western blot analyses

All samples were boiled for 5 min in 2% SDS loading buffer before proteins were separated on 10% SDS-polyacrylamide mini gels. After electrophoresis, proteins were either stained with Coomassie blue or electrotransferred onto a nitrocellulose membrane (Bio-Rad). Polyclonal rabbit antisera against OprD (1:2000) and XcpY (1:1000) were used for the detection of outer and inner membrane proteins, respectively. Goat anti-rabbit alkaline horseradish peroxidase-conjugated secondary antibodies and enhanced chemiluminescence Western blotting reagents (Bio-Rad) were used for protein detection.

LPS dot blot analysis

Aliquots of vesicles were adsorbed onto a nitrocellulose membrane using a dot blot apparatus (Bio-Rad). The membrane was treated as for the Western blot analyses, using goat polyclonal antibodies directed against lipid A (Thermo Fisher Scientific) at a dilution of 1:5000 followed by rabbit anti-goat alkaline horseradish peroxidase-conjugated secondary antibodies (Thermo Fisher Scientific).

Cryo-electron microscopy

Samples for cryo-EM were prepared as described above for the isolation of extracellular vesicles. Quantifoil® gold finder grids R2/2 (Au G200F1, Quantifoil Micro Tools) were glow-discharged with plasma. No fiducial markers were added. Three miroliters of the sample (containing ~150 µg of proteins per ml) was applied to the front and 1 µl to the back of each grid. For optimal results, samples were dispensed directly from the side window of the environmental chamber immediately before blotting. Grids were blotted for 3 s and vitrified in precooled liquid ethane with a Leica GP automatic plunge freezer. The grids were then transferred to the NanoSoft clipping station and clipped to ensure compatibility with the cryo-EM autoloader. Samples were studied at SOLEIL using the POLARIS cryo-electron microscope, a 300 keV Titan Krios G4 (Thermo Fisher Scientific) equipped with a Falcon 4i detector and a Selectris X energy filter. Cryo-ET data collections were recorded in low-dose imaging conditions, with a maximum dose per tomogram in the 100–140 $e^{-}/Å^2$ range, at a magnification of ×130,000, corresponding to a pixel size of 0.96 Å. Vesicle size and morphology were analyzed using ImageJ.

Chemical synthesis of Cu-NV716

Four milligrams of NV716 was dissolved in 2 ml of 96% ethanol in a 10 ml round-bottom flask, then a solution of $CuSO_4$ (1.8 mg dissolved in 2 ml of 96% ethanol) was added. The mixture was heated under reflux for 5 h. After concentration under reduced pressure, a blue-green Cu-NV716 complex

was obtained. A 10 mM working solution was prepared by dissolving the complex in 1 ml of deionized water.

X-ray fluorescence nano-imaging and image analysis

Bacteria were grown to the mid-exponential phase and exposed to NaPi buffer ± NV716-Cu (10 µM final) as described for TEM analyses. For each condition (control vs. NV716-Cu treatment), bacterial suspension (2 µl) was spotted on silicon nitride membranes (Silson Ltd, England) with a size of $1.5 \times 1.5\ mm^2$ and a thickness of 500 nm before blotting to remove excess media. Membranes were plunge-frozen in liquid ethane using a Leica EM GP2 automatic plunge freezer. Vitrified samples were transferred to a cryo-box in a Leica EM VCM vacuum cryo-manipulation system and kept in liquid nitrogen until analysis. Experiments were conducted under vacuum (~$1e^{-7}$ mbar) in cryogenic conditions on the Nano-Imaging beamline ID16A of the ESRF[71]. The X-ray excitation energy was set to 17 keV, and all relevant elements were detected using their K-level emission lines. A multilayer coated fixed curvature Kirkpatrick-Baez (KB) focusing mirror system provides the nano focus (~30 nm) and a high flux of 4.1×10^{11} ph/s from 1% of the broad passband[72]. Nano-XRF measurements were performed with a step size of 20 nm/pixel or 40 nm/pixel and an integration time of 50 ms/pixel. The XRF signal was recorded with two large solid-angle detectors, based on multi-element silicon drift diodes, placed at approximately 90° at either side of the incident beam.

Galleria mellonella infection model

The synergy between DOX and NV716 was assessed in the *G. mellonella* infection model. The larvae of *G. mellonella* (INRAE, Jouy-en-Josas, France) were randomly divided into four groups ($n = 20$ per group) and infected with 10 µl of a *P. aeruginosa* suspension (PAO1, 25 CFU) or left uninfected. After 1 h post-infection, the infected larvae were treated with NaPi buffer, DOX (50 mg/Kg) with or without NV716 (5 µM). Survival rates were recorded for 3 days.

ADMET study

The characterized molecule was designed in the MarvinSketch® academic license software of the ChemAxon© for theoretical calculation of the physicochemical properties of ionization (pKa), partition coefficient (logP), distribution coefficient (logD), water solubility (logS), and polarity (PSA), used as molecular descriptors for pharmacokinetic properties. Then, the SMILES of NV716 [C/C(CC/C=C(CC/C=C(C)/C)/C)=C\CNCCCNCCCCNCCCN] was uploaded to the online server ADMETlab (https://admetmesh.scbdd.com/)[48] for consensual prediction of pharmacokinetic properties of absorption, distribution, metabolism, excretion, and toxicity (ADMET) models.

Determination of lipid A modification

Lipid A was prepared and analyzed for modifications by tandem mass spectrometry (LC-MS/MS) at LPS Biosciences (Orsay, France) as described previously[73].

Statistical analyses

Statistical analyses were performed using GraphPad Prism 10. All data are presented as means and standard deviations.

Data availability

The data supporting the findings of this study are available within the article and its Supplementary Information files. Source data underlying the figures are provided as Supplementary Data 1–7. ADMET predictions are provided as Supplementary Data 8. Additional data and code have been deposited in Zenodo (https://doi.org/10.5281/zenodo.17751668).

Code availability

The code used for the analysis of antibiotic accumulation in bacteria is available at: https://gitlab.synchrotron-soleil.fr/disco-beamline/bacteria-drug-uv-analysis.

Received: 14 January 2026; Accepted: 9 April 2026;
Published online: 30 April 2026

References

1. Silver, L. L. A Gestalt approach to Gram-negative entry. *Bioorg. Med. Chem.* **24**, 6379–6389 (2016).
2. Payne, D. J., Gwynn, M. N., Holmes, D. J. & Pompliano, D. L. Drugs for bad bugs: confronting the challenges of antibacterial discovery. *Nat. Rev. Drug Discov.* **6**, 29–40 (2007).
3. Silver, L. L. Challenges of antibacterial discovery. *Clin. Microbiol. Rev.* **24**, 71–109 (2011).
4. O'Neill, J. *Tackling Drug-resistant Infections Globally: Final Report and Recommendations* (Government of the United Kingdom, 2016).
5. Tacconelli, E. et al. Discovery, research, and development of new antibiotics: the WHO priority list of antibiotic-resistant bacteria and tuberculosis. *Lancet Infect. Dis.* **18**, 318–327 (2018).
6. Yoshimura, F. & Nikaido, H. Permeability of *Pseudomonas aeruginosa* outer membrane to hydrophilic solutes. *J. Bacteriol.* **152**, 636–642 (1982).
7. Nikaido, H. Molecular basis of bacterial outer membrane permeability revisited. *Microbiol. Mol. Biol. Rev.* **67**, 593–656 (2003).
8. Tamber, S., Ochs, M. M. & Hancock, R. E. Role of the novel OprD family of porins in nutrient uptake in *Pseudomonas aeruginosa*. *J. Bacteriol.* **188**, 45–54 (1988).
9. Ude, J. et al. Outer membrane permeability: antimicrobials and diverse nutrients bypass porins in *Pseudomonas aeruginosa*. *Proc. Natl. Acad. Sci. USA* **118**, e2107644118 (2021).
10. Li, X. Z. et al. The challenge of efflux-mediated antibiotic resistance in Gram-negative bacteria. *Clin Microbiol. Rev.* **28**, 337–418 (2015).
11. Lin, X. Z., Plésiat, P. & Nikaido, H. Interplay between the MexA-MexB-OprM multidrug efflux system and the outer membrane barrier in the multiple antibiotic resistance of *Pseudomonas aeruginosa*. *J. Antimicrob. Chemother.* **45**, 433–436 (2000).
12. Krishnamoorthy, G. et al. The synergy between active efflux and outer membrane diffusion defines the rules of antibiotic permeation into Gram-negative bacteria. *mBio* **8**, e01172–17 (2017).
13. Botelho, J., Grosso, F. & Peixe, L. Antibiotic resistance in *Pseudomonas aeruginosa* - Mechanisms, epidemiology and evolution. *Drug Resist. Update* **44**, 100640 (2019).
14. Diani, E., Bianco, G., Gatti, M., Gibellini, D. & Gaibani, P. Colistin: lights and shadows of an older antibiotic. *Molecules.* **29**, 2969 (2024).
15. Avent, M. L., Rogers, B. A., Cheng, A. C. & Paterson, D. L. Current use of aminoglycosides: indications, pharmacokinetics, and monitoring for toxicity. *Intern. Med. J.* **41**, 441–449 (2011).
16. Sjuts, H. et al. Molecular basis for inhibition of AcrB multidrug efflux pump by novel and powerful pyranopyridine derivatives. *Proc. Natl. Acad. Sci. USA* **113**, 3509–3514 (2016).
17. Plé, C. et al. Pyridylpiperazine-based allosteric inhibitors of RND-type multidrug efflux pumps. *Nat. Commun.* **13**, 115 (2022).
18. Compagne, N. et al. Update on the discovery of efflux pump inhibitors against critical priority Gram-negative bacteria. *Antibiotics* **12**, 180 (2023).
19. MacNair, C. R. & Brown, E. D. Outer membrane disruption overcomes intrinsic, acquired, and spontaneous antibiotic resistance. *mBio* **11**, e01615–e01620 (2020).
20. MacNair, C. R. et al. Preclinical development of pentamidine analogs identifies a potent and nontoxic antibiotic adjuvant. *ACS Infect. Dis.* **8**, 768–777 (2022).
21. Klobucar, K. & Brown, E. D. New potentiators of ineffective antibiotics: targeting the Gram-negative outer membrane to overcome intrinsic resistance. *Curr. Opin. Chem. Biol.* **66**, 102099 (2022).
22. Brunel, J. M., Lieutaud, A., Lome, V., Pagès, J. M. & Bolla, J. M. Polyamino geranic derivatives as new chemosensitizers to combat antibiotic-resistant Gram-negative bacteria. *Bioorg. Med. Chem.* **21**, 1174–1179 (2013).

23. Borselli, D. et al. Polyamino-isoprenic derivatives block intrinsic resistance of *P. aeruginosa* to doxycycline and chloramphenicol in vitro. *PLoS ONE* **11**, e0154490 (2016).
24. Lieutaud, A., Pieri, C., Bolla, J. M. & Brunel, J. M. New polyaminoisoprenyl antibiotics enhancers against two multidrug-resistant Gram-negative bacteria from *Enterobacter* and *Salmonella* species. *J. Med. Chem.* **63**, 10496–10508 (2020).
25. Wang, G., Brunel, J. M., Bolla, J. M. & Van Bambeke, F. The polyaminoisoprenyl potentiator NV716 revives old disused antibiotics against intracellular forms of infection by *Pseudomonas aeruginosa*. *Antimicrob. Agents Chemother.* **65**, e02028–20 (2021).
26. Wang, G. et al. The membrane-active polyaminoisoprenyl compound NV716 re-sensitizes *Pseudomonas aeruginosa* to antibiotics and reduces bacterial virulence. *Commun. Biol.* **5**, 871 (2022).
27. Davis, T. D., Gerry, C. J. & Tan, D. S. A general platform for systematic quantitative evaluation of small-molecule permeability in bacteria. *ACS Chem. Biol.* **9**, 2535–2544 (2014).
28. Richter, M. F. et al. Predictive compound accumulation rules yield a broad-spectrum antibiotic. *Nature* **545**, 299–304 (2017).
29. Iyer, R. et al. Evaluating LC-MS/MS to measure the accumulation of compounds within bacteria. *ACS Infect. Dis.* **4**, 1336–1345 (2018).
30. Vergalli, J. et al. The challenge of intracellular antibiotic accumulation, a function of fluoroquinolone influx versus bacterial efflux. *Commun. Biol.* **3**, 98 (2020).
31. Masi, M. et al. Cephalosporin translocation across enterobacterial OmpF and OmpC channels, a filter across the outer membrane. *Commun. Biol.* **5**, 1059 (2022).
32. Geddes, E. J. et al. Porin-independent accumulation in *Pseudomonas* enables antibiotic discovery. *Nature* **624**, 145–153 (2023).
33. Hirai, K., Aoyama, H., Irikura, T., Iyobe, S. & Mitsuhashi, S. Differences in susceptibility to quinolones of outer membrane mutants of *Salmonella typhimurium* and *Escherichia coli*. *Antimicrob. Agents Chemother.* **29**, 535–538 (1986).
34. Hancock, R. E. & Bell, A. Antibiotic uptake into Gram-negative bacteria. *Eur. J. Clin. Microbiol. Infect. Dis.* **7**, 713–720 (1988).
35. Delcour, A. H. Outer membrane permeability and antibiotic resistance. *Biochim. Biophys. Acta.* **1794**, 808–816 (2009).
36. Nikaido, H. & Thanassi, D. G. Penetration of lipophilic agents with multiple protonation sites into bacterial cells: tetracyclines and fluoroquinolones as examples. *Antimicrob. Agents Chemother.* **37**, 1393–1399 (1993).
37. Okusu, H., Ma, D. & Nikaido, H. AcrAB efflux pump plays a major role in the antibiotic resistance phenotype of *Escherichia coli* multiple-antibiotic-resistance (Mar) mutants. *J. Bacteriol.* **178**, 306–308 (1996).
38. Li, X. Z., Livermore, D. M. & Nikaido, H. Role of efflux pump(s) in intrinsic resistance of *Pseudomonas aeruginosa*: resistance to tetracycline, chloramphenicol, and norfloxacin. *Antimicrob. Agents Chemother.* **38**, 1732–1741 (1994).
39. Masuda, N. et al. Substrate specificities of MexAB-OprM, MexCD-OprJ, and MexXY-OprM efflux pumps in *Pseudomonas aeruginosa*. *Antimicrob. Agents Chemother.* **44**, 3322–3327 (2000).
40. Leus, I. V. et al. Functional diversity of Gram-negative permeability barriers reflected in antibacterial activities and intracellular accumulation of antibiotics. *Antimicrob. Agents Chemother.* **67**, e0137722 (2023).
41. Vergalli, J. et al. Spectrofluorimetric quantification of antibiotic drug concentration in bacterial cells for the characterization of translocation across bacterial membranes. *Nat. Protoc.* **13**, 1348–1361 (2018).
42. Troudi, A. et al. Efficiency of a tetracycline-adjuvant combination against multidrug-resistant *Pseudomonas aeruginosa* Tunisian clinical isolates. *Antibiotics* **9**, 919 (2020).
43. Needham, B. D. & Trent, M. S. Fortifying the barrier: the impact of lipid A remodeling on bacterial pathogenesis. *Nat. Rev. Microbiol.* **11**, 467–481 (2013).
44. Olaitan, A. O., Morand, S. & Rolain, J. M. Mechanisms of polymyxin resistance: acquired and intrinsic resistance in bacteria. *Front. Microbiol.* **5**, 643 (2014).
45. Ault-Riché, D., Fraley, C. D., Tzeng, C. M. & Kornberg, A. Novel assay reveals multiple pathways regulating stress-induced accumulations of inorganic polyphosphate in *Escherichia coli*. *J. Bacteriol.* **180**, 1841–1847 (1998).
46. Magkiriadou, S., Stepp, W. L., Newman, D. K., Manley, S. & Racki, L. R. Polyphosphate affects cytoplasmic and chromosomal dynamics in nitrogen-starved *Pseudomonas aeruginosa*. *Proc. Natl. Acad. Sci. USA* **121**, e2313004121 (2024).
47. Racki, L. R. et al. Polyphosphate granule biogenesis is temporally and functionally tied to cell cycle exit during starvation in *Pseudomonas aeruginosa*. *Proc. Natl. Acad. Sci. USA* **114**, E2440–E2449 (2017).
48. Xiong, G. et al. ADMETlab 2.0: an integrated online platform for accurate and comprehensive predictions of ADMET properties. *Nucleic Acids Res.* **49**, W5–W14 (2021).
49. Bisht, R., Charlesworth, P. D., Sperandeo, P. & Polissi, A. Breaking barriers: exploiting envelope biogenesis and stress responses to develop novel antimicrobial strategies in Gram-negative bacteria. *Pathogens* **13**, 889 (2024).
50. Rouvier, F., Brunel, J. M., Pagès, J. M. & Vergalli, J. Efflux-mediated resistance in *Enterobacteriaceae*: recent advances and ongoing challenges to inhibit bacterial efflux pumps. *Antibiotics* **14**, 778 (2025).
51. Wesseling, C. M. J. & Martin, N. I. Synergy by perturbing the Gram-negative outer membrane: opening the door for Gram-positive specific antibiotics. *ACS Infect. Dis.* **8**, 1731–1757 (2022).
52. Adams, J. M. E., Moulding, P. B. & El-Halfawy, O. M. Polyamine-mediated sensitization of *Klebsiella pneumoniae* to macrolides through a dual mode of action. *ACS Infect. Dis.* **10**, 2183–2195 (2024).
53. Draveny, M. et al. Scope and limitations of exploiting the ability of the chemosensitizer NV716 to enhance the activity of tetracycline derivatives against *Pseudomonas aeruginosa*. *Molecules.* **28**, 4262 (2023).
54. Sabnis, A. et al. Colistin kills bacteria by targeting lipopolysaccharide in the cytoplasmic membrane. *Elife.* **10**, e65836 (2021).
55. Baijal, K. et al. Polyphosphate kinase regulates LPS structure and polymyxin resistance during starvation in *E. coli*. *PLoS Biol.* **22**, e3002558 (2024).
56. Cain, B. N. & Hergenrother, P. J. Using permeation guidelines to design new antibiotics: a PASsagE into *Pseudomonas aeruginosa*. *Clin. Transl. Med.* **14**, e1600 (2024).
57. Hoegy, F., Mislin, G. L. & Schalk, I. J. Pyoverdine and pyochelin measurements. *Methods Mol. Biol.* **1149**, 293–301 (2014).
58. Gasser, V. et al. The esterase PfeE, the Achilles' heel in the battle for iron between *Pseudomonas aeruginosa* and *Escherichia coli*. *Int. J. Mol. Sci.* **22**, 2814 (2021).
59. Desmarais, S. M. et al. High-throughput, highly sensitive analyses of bacterial morphogenesis using ultra-performance liquid chromatography. *J. Biol. Chem.* **290**, 31090–31100 (2015).
60. Giuliani, A. et al. DISCO: a low-energy multipurpose beamline at synchrotron SOLEIL. *J. Synchrotron. Radiat.* **16**, 835–841 (2009).
61. Jamme, F. et al. Synchrotron UV fluorescence microscopy uncovers new probes in cells and tissues. *Microsc. Microanal.* **16**, 507–514 (2010).
62. Schmidt, U. et al. (eds) Medical image computing and computer-assisted intervention—MICCAI 2018. In *Proc. Lecture Notes in Computer Science* 11071 (Springer, 2018).
63. Wood, S. J., Miller, K. A. & David, S. A. Anti-endotoxin agents. Development of a fluorescent probe displacement method optimized for the rapid identification of lipopolysaccharide-binding agents. *Comb. Chem. High Throughput Screen.* **7**, 239–249 (2004).
64. Sorrentino, A. et al. MISTRAL: a transmission soft X-ray microscopy beamline for cryo nano-tomography of biological samples and magnetic domains imaging. *J. Synchrotron Radiat.* **22**, 1112–1117 (2015).

65. Loconte, V. et al. Soft X-ray tomography to map and quantify organelle interactions at the mesoscale. *Structure* **30**, 510–521.e3 (2022).
66. Otón, J. et al. Characterization of transfer function, resolution and depth of field of a soft X-ray microscope applied to tomography enhancement by Wiener deconvolution. *Biomed. Opt. Express* **7**, 5092–5103 (2016).
67. Zheng, S. et al. AreTomo: An integrated software package for automated marker-free, motion-corrected cryo-electron tomographic alignment and reconstruction. *J. Struct. Biol. X* **6**, 100068 (2022).
68. Kremer, J. R., Mastronarde, D. N. & McIntosh, J. R. Computer visualization of three-dimensional image data using IMOD. *J. Struct. Biol.* **116**, 71–76 (1996).
69. Agulleiro, J. I. & Fernandez, J. J. Tomo3D 2.0-exploitation of advanced vector extensions (AVX) for 3D reconstruction. *J. Struct. Biol.* **189**, 147–152 (1995).
70. Edelstein, A. D. et al. Advanced methods of microscope control using μManager software. *J. Biol. Methods* **1**, e10 (2014).
71. da Silva, J. C. et al. Efficient concentration of high-energy X-rays for diffraction-limited imaging resolution. *Optica* **4**, 492–495 (2017).
72. Morawe, C. B. R. et al. Graded multilayers for figured Kirkpatrick-Baez mirrors on the new ESRF end station ID16A. In *Proc. Advances in X-ray/EUV Optics and Components* San Diego, CA, USA (SPIE, 2015).
73. Latino, L., Caroff, M. & Pourcel, C. Fine structure analysis of lipopolysaccharides in bacteriophage-resistant *Pseudomonas aeruginosa* PAO1 mutants. *Microbiology* **163**, 848–855 (2017).

Acknowledgements

We thank Dianne K. Newman and Isabelle Schalk for sharing bacterial strains, and Bérengère Ize for the gift of anti-XcpY antibodies. We acknowledge financial support from the Cystic Fibrosis Foundation (Grant SINGH24R0), which maintains the Pseudomonas aeruginosa PAO1 mutant collection. TEM experiments were performed at the Imagery Unit platform (Institut de Recherche Biomédicale des Armées) with support from the IRBA staff, especially Cécile Enfroy and Cédric Castellarin. STEM-EDX experiments were performed at the CIMEX platform (Institut Polytechnique de Paris, France) with support from the CIMEX staff. DUV imaging experiments were performed at the DISCO beamline of SOLEIL under proposals 20221408 and 20230506. Cryo-SXT experiments were performed at the MISTRAL beamline at ALBA under proposals 2021095475 and 2023027319, with assistance from Eva Pereiro. Cryo-nanoXRF experiments were performed at the ID16A beamline of ESRF under proposal MD-1382, with assistance from Peter Cloetens. Cryo-EM experiments were performed at SOLEIL with support from the POLARIS staff under proposal 99250126. M.D. was supported by a Ph.D. contract funded by SOLEIL. M.N. and J.-M.B. received funding from the Agence Nationale de la Recherche (ANR-19-CE44-0015). A.D.-P. was supported by an apprenticeship agreement funded by SOLEIL.

Author contributions

F.J. and M.M. conceived and supervised the project. M.D. performed the majority of the experiments. M.D. and M.N. conducted antibiotic susceptibility assays. F.J., M.D., and V.R. prepared samples for ALBA and ESRF. H.C. and M.D. performed experiments on the DISCO beamline at SOLEIL. F.J., H.C., M.D., M.M., M.N., and V.R. conducted experiments at ALBA and ESRF. A.-L.F. performed TEM, and A.-L.F. and M.G. performed STEM-EDX experiments. A.D.-P., M.D., and M.M. performed biochemical characterization of extracellular vesicles. M.M., H.R., and F.J. prepared samples for cryo-EM, and P.L. acquired cryo-EM images. M.D. and F.N.-R. conducted animal infection models. J.-M.B. carried out and described the chemical synthesis of NV716 and Cu–NV716. F.J., H.C., M.D., and M.M. performed data analysis. M.M. wrote the manuscript. F.J., H.C., J.-M.B., M.D., and M.M. reviewed the manuscript. All authors read and approved the final manuscript.

Competing interests

The authors declare no competing interests.

Additional information

Supplementary information The online version contains supplementary material available at https://doi.org/10.1038/s44259-026-00203-w.

Correspondence and requests for materials should be addressed to Muriel Masi.